Available online at www.sciencedirect.com
SCIENCE DIRECT®
Journal of Nuclear Materials 336 (2005) 145–155
journal of nuclear materials
www.elsevier.com/locate/jnucmat

Elastic behavior of porous ceramics: application to nuclear fuel materials

J.-M. Gatt [a], Y. Monerie [a,*], D. Laux [a], D. Baron [b]

[a] CEA Cadarache DEN/DEC/SESC, 13108 Saint-Paul lez Durance, France
[b] EDF/DRD/MMC Renardière, 77250 Moret sur Loing, France

Received 30 October 2003; accepted 1 September 2004

Abstract

This study deals with the determination of effective elastic properties of random porous ceramics. Ceramic-matrix composites with bi-modal pore shape (spherical and ellipsoidal pores randomly distributed) are considered. For such a microstructure, various micro-mechanical estimates are compared to three dimensional numerical simulations based on periodic homogenization. Effective elastic moduli are derived as a function of matrix properties, porosity and pore shape. In the case of nuclear fuel ceramics, spherical and ellipsoidal pores are identified to inter-granular and intra-granular pores respectively, and obtained effective elastic properties are compared to experimental micro-acoustic data.

PACS: 62.20.D; 46.90; 43.85; 28.00

1. Introduction

This paper is devoted to the determination of overall elastic properties of random porous ceramics with a particular interest for nuclear fuel materials. In particular, we attempt to check by micro-mechanical approaches the accuracy of fits given in literature for elastic properties of UO_2 fuel material [9]. This type of porous ceramic-matrix material is assumed to contain both inter-granular spherical pores at the nanometric scale and intra-granular ellipsoidal pores at the micrometric scale.

Under the assumption that each class of pores is spatially uncorrelated and randomly distributed, an accurate numerical estimate of random porous media containing non-overlapping ellipsoidal pores is established in Section 2. From a numerical point of view and following [15], a technique of periodic homogenization specifically designed for random porous media is implemented in a finite element code. Sensitivity of numerical results with respect to the size of the representative volume element (RVE), to the finite element discretization and to the sampling process is addressed. From a mechanical point of view, effects of porosity and aspect ratio of pores (oblate, prolate and spherical pores) are investigated.

In Section 3, various analytical estimates (such as Berryman self-consistent estimate [2], Mori–Tanaka estimate [12] and the Ponte-Castañeda and Willis estimate [14]) are compared to numerical results. The classical self-consistent estimate is shown to be the most accurate model for the considered microstructures.

Section 4 is devoted to experimental results on UO_2 fuel material. A micro-acoustic approach is used to

* Corresponding author. Present address: CE Cadarache IRSN/DPAM/SEMCA, 13108 Saint-Paul lez Durance, France.

0022-3115/$ - see front matter
doi:10.1016/j.jnucmat.2004.09.009

determine elastic properties of this material with an initial porosity up to 20%. Our experimental data, our numerical computations and the results obtained with the self-consistent estimate are compared in Section 5 to the commonly used Martin's approximate [9]. The effect of the coexistence of spherical and ellipsoidal pores at different scales is addressed in terms of convenient aspect ratio for ellipsoidal pores.

2. Numerical estimate of effective elastic moduli

Following [15], we propose in this section a three dimensional numerical estimate of random porous ceramics based on periodic homogenization. When seeking the effective properties of elastic media, one can solve the local equations of elasticity using a finite element code over a large RVE. But, due to statistical representation, the size of such a convenient RVE often leads to unreasonable computational time. To face this difficulty, the solution undertaken in this work consists first in choosing smaller RVEs reproduced by periodicity and then in averaging the numerical results over many RVE realizations. The characteristic size of RVE leading to macroscopically isotropic effective porous material over a reasonable number of realizations is investigated further in this paper.

In the following, only quasi-static evolutions are considered, body forces are neglected and displacements and strains are considered to be small.

2.1. Computational method

The technique of periodic homogenization (see [11] and references therein) is implemented on the finite element code CAST3M. Within the strain approach framework, this method can be briefly summarized as follows.

For a periodic geometry obtained by periodic translation of a RVE Y submitted to an overall prescribed strain E, the local fields of stress σ and strain $\varepsilon(u)$ (where u denotes the displacement field) are also Y-periodic. The fluctuating part $\varepsilon(u')$ of $\varepsilon(u)$ around its constant part E, i.e. $\varepsilon(u) = E + \varepsilon(u')$, is derived from a periodic displacement field u'. This decomposition implies in particular that $\langle \varepsilon(u') \rangle = 0$ and $\langle \varepsilon(u) \rangle = E$, where the brackets $\langle \cdot \rangle$ denotes the average of a field on the RVE.

Denoting by c the local stiffness and by v the outer unit vector of Y, the local problem reads for any prescribed macroscopic strain E:

$$(P_E)\begin{cases} \operatorname{div}(\sigma) = 0, & \text{in } Y, \\ \sigma = c : (E + \varepsilon(u')), & \text{in } Y, \\ u' \text{ periodic, and } \sigma \cdot v \text{ anti-periodic}, & \text{on } \partial Y, \end{cases} \tag{1}$$

where ∂Y denotes the outer boundary of Y.

The effective stiffness C is then obtained by the following relation: $C : E = \Sigma = \langle \sigma \rangle = \langle c : (E + \varepsilon(u')) \rangle$, where Σ is the overall stress field. A convenient way to compute this effective stiffness C is to solve six elementary problems (P_E) corresponding to six different generalized loadings E related to three tractions and three shears. Denoting by u'^{kh} the solution of the problem (P_E) with $E = I^{kh}$ (where $I^{kh}_{ij} = 1/2(\delta_{ik}\delta_{jh} + \delta_{ih}\delta_{jk})$ is the fourth-order identity tensor, and δ denotes the Kronecker symbol), the stiffness C is obtained by linear combinations ($E = E_{kh} I^{kh}$):

$$C_{ijkh} = \left\langle c_{ijpq}\left(I^{kh}_{pq} + \varepsilon_{pq}(u'^{kh})\right)\right\rangle. \tag{2}$$

These six problems are solved on a cubic RVE applying the following periodic boundary conditions (s denotes the length of an edge):

$$\begin{cases} u(x,0,z) = u(x,s,z), & \forall (x,z) \in [0,s]^2, \\ u(0,y,z) = u(s,y,z), & \forall (y,z) \in [0,s]^2, \\ u(x,y,0) = u(x,y,s), & \forall (x,y) \in [0,s]^2. \end{cases} \tag{3}$$

In the proposed computational model, particular attention has to be focused on two main sources of errors: first, the mismatch on overall isotropy due to a periodic RVE-based modeling for random media, and second, the classical discretization error.

As regards the first point, it is worth noting that the elastic properties are length scale invariant: our computational method applies to pores of any characteristic length for which the continuum assumption holds. Briefly, the problem is to mimic the random microstructure of an isotropic material using a periodic RVE including a random distribution of cavities. Two different situations can lead to an accurate estimate of the elastic tensor C: few realizations of random distributions in a large RVE (i.e. including a large number of pores) or numerous realizations in a small RVE. An isotropy criterion has to be used to evaluate the accuracy of the modeling. Introducing the classical isotropy basis $J = 1/3 i \otimes i$ (where $\otimes$ denotes the tensor product, and $i_{ij} = \delta_{ij}$) and $K = I - J$, a measure of the overall isotropy of a RVE is given for any non-zero tensor C by

$$\varsigma(C) = 1 - \frac{\|C - \operatorname{Proj}_{\{J,K\}}(C)\|}{\|C\|}, \tag{4}$$

$$\operatorname{Proj}_{\{J,K\}}(C) = \left(\frac{(C :: J)}{J :: J} J + \frac{(C :: K)}{K :: K} K\right), \tag{5}$$

where $\|\cdot\|$ denotes any quadratic norm, and $\operatorname{Proj}_{\{J,K\}}(C)$ being the projection of C on the isotropy basis.

In the case of few realizations over a large RVE, it is time consuming to evaluate C_i at each realization (C_i is the elastic tensor at the ith sample) but $\varsigma\left(\frac{1}{N}\sum_{i=1}^{N} C_i\right)$ rapidly tends to one (perfect isotropy) with the number N of

realizations. In case of numerous realizations over a small RVE, C_i is quickly computed at each realization but $\varsigma\left(\frac{1}{N}\sum_{i=1}^{N} C_i\right)$ tends to one only for a large number of realizations. Our numerical computations show that a satisfactory compromise is reached with about four realizations of RVE containing 15 pores: overall isotropy is then more than 99% for spherical pores and more than 98% for ellipsoidal pores (with w ranging from 0.1 to 10).

Our random realizations are based upon a 'quasi-dead leaves process': a non-overlapping spherical volume is prescribed around each ellipsoid corresponding to the inscribed sphere in the ellipsoid. In the particular case of spherical pores, this process tends to an hard-core point process. In what follows, we denote by A the length of the semi-axis of symmetry of the ellipsoidal pores, by R the length of each semi-axis perpendicular to the symmetry axis, and by $w = A/R$ the aspect ratio of the ellipsoids ($w < 1$ for oblates, and $w > 1$ for prolates).

Periodic geometric boundary conditions are taken into account, and the intersections between pores and boundaries of RVE are also periodic (see Fig. 1).

To evaluate the discretization errors, simulations are performed at $f = 10\%$ (f is the porosity) for various numbers of elements M by RVE edges (uniform mesh of linear cubic 'Q1' finite elements in 3D). This analysis is conducted for several aspect ratios w ($w = 0.1, 0.25, 0.5, 1, 2, 4, 10$). Results are plotted on Fig. 2 in the case of spherical cavities. We obtain that effective elastic moduli can be approached for a given porosity by Eq. (6):

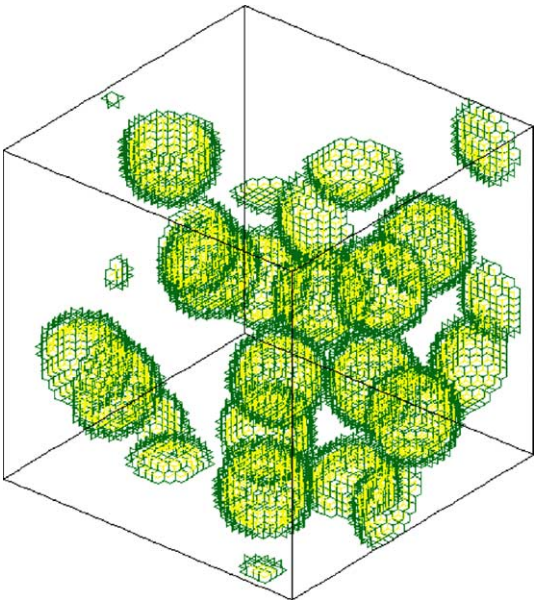

Fig. 1. Examples of meshing of spherical cavities for random samples.

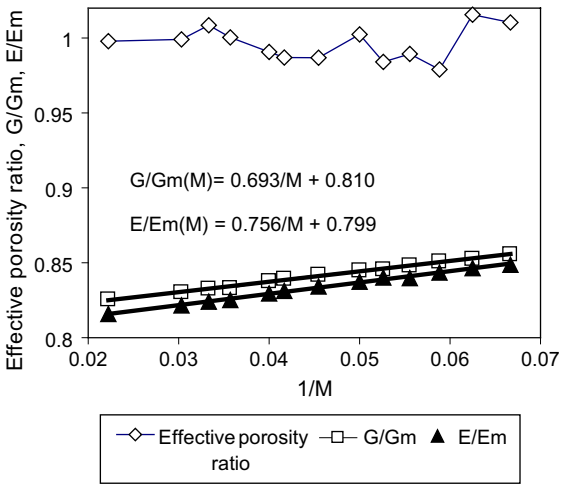

Fig. 2. Effect of the mesh parameter M on the effective porosity ratio ($f_{\text{obtained}}/f_{\text{prescribed}}$) and on effective elastic moduli (spherical cavities, $f_{\text{prescribed}} = 10\%$). For each value of M, effective elastic stiffness is the average upon four samples with 15 pores (resulting isotropy about 99%). The effective porosity ratio is plotted for the more anisotropic result on the four samples.

$$\begin{cases} \dfrac{E}{E_m}(w) \approx \dfrac{E}{E_m}(w, M) - a_E(w)\dfrac{1}{M}, \\ \dfrac{G}{G_m}(w) \approx \dfrac{G}{G_m}(w, M) - a_G(w)\dfrac{1}{M}, \end{cases} \tag{6}$$

where E and G denote respectively the effective Young and the effective shear moduli of the porous material, E_m and G_m denote respectively the Young and the shear moduli of the matrix and $a_E(w)$ and $a_G(w)$ are non-negative functions of w.

Same conclusions were formulated by [16] for the Young modulus in the case of spherical inclusions and for porosity varying between 10% and 50%. These affine relations with respect to $1/M$ are here confirmed even for ellipsoidal pores and extended to the shear modulus.

Following [15], the effective elastic moduli are then computed for three different values of M (according to Fig. 2, $M > 33$ for a convenient estimate of the inner porosity) and extrapolated to $M \to \infty$. For each value of M, the effective elastic tensor is determined by averaging the results of $N = 4$ samples (i.e. 12 computations of a periodic elastic problem for each porosity and for each aspect ratio). As required, the final effective elastic tensor is almost perfectly isotropic, and elastic moduli are deduced by projection on the isotropy basis (J, K).

2.2. Numerical results for spherical cavities

Fig. 3 shows the evolution of the Young modulus and the shear modulus versus porosity. Table 1 shows at $f = 10\%$ a comparison between our numerical results and the numerical results of [15]. Differences between

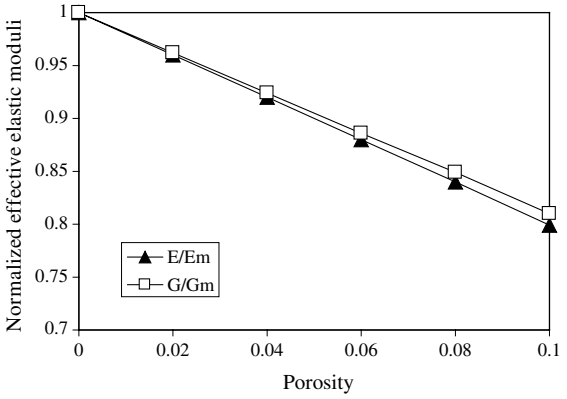

Fig. 3. Effective elastic moduli versus porosity (spherical cavities): numerical results.

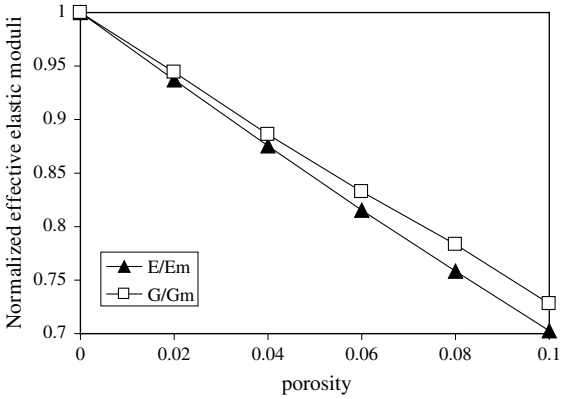

Fig. 4. Numerical results for ellipsoidal pores ($w = 0.2$): normalized effective elastic moduli versus porosity.

our simulations and those of [15] could be explained by the realization process: in the current study, hard-core point problem is considered whereas overlapping spheres are used in [15].

2.3. Numerical results for ellipsoidal cavities

Although the percolation threshold is estimated at $f_p = 28.54\%$ for overlapping spheres [5], lower porosities have to be considered for ellipsoidal pores: a percolation threshold of $f_p = 10\%$ is reached for $w = 0.1$ in the oblate case and for $w = 10$ in the prolate case [5]. Numerical estimates of elastic moduli are given as a function of porosity on Fig. 4 for $w = 0.2$, and as a function of the aspect ratio on Fig. 5 for $f = 10\%$.

The moduli exhibit a maximum obtained when the shape is spherical. In the oblate case, elastic moduli monotonously decrease with respect to w. The limit case of disk-shaped inclusions given by [21] confirms that for pores, the elastic moduli tend to zero when w tends to zero. In the prolate case, the numerical results show that an asymptote is reached for large w. The limit model of [21] for needle shaped inclusions gives $E/E_m(w \to \infty) \to 0.769$ and $G/G_m(w \to \infty) \to 0.783$ for 10% of porosity. At $w = 10$ and 10% of porosity, we found $E/E_m(w = 10) \approx 0.773$ and $G/G_m(w = 10) \approx 0.788$. In the case of oblate pores with $w = 0.25$, our results are numerically compared in Table 2 to those of [15]. A small difference of 1% is observed (order of magnitude of the uncertainties) due to the difference in the realization process (quasi-overlapping process and real overlapping process).

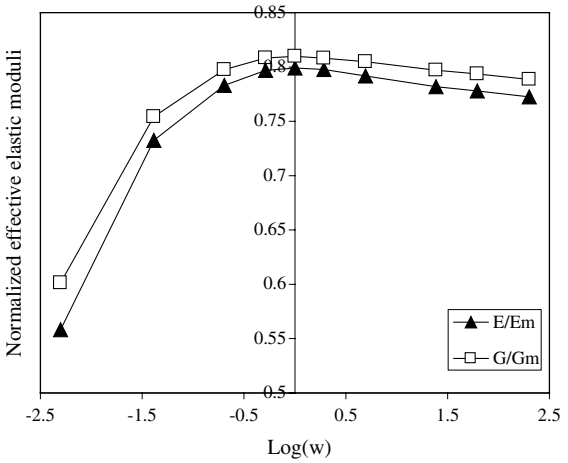

Fig. 5. Numerical results for spherical and ellipsoidal pores at $f = 10\%$: normalized effective elastic moduli versus aspect ratio. The simulations were performed for w lying between 0.1 and 10 respectively, which are the percolation thresholds for oblate and prolate pores respectively at $f = 10\%$ [5].

In the next section, various classical analytical estimates are compared to numerical results in order to determine the most accurate analytical estimate for the considered type of microstructure.

Table 1
Spherical pores at $f = 10\%$: comparison between numerical results (hard-core point process), numerical results of [15] (overlapping pores) and various analytical approaches

	Numerical results	Roberts–Garboczi	Self-consistent	Mori–Tanaka	Dilute case	Wu's model	Differential scheme
E/E_m	0.799	0.806	0.800	0.818	0.798	0.800	0.818
G/G_m	0.810	0.814	0.810	0.827	0.812	0.811	0.828

Table 2
Numerical solution for ellipsoidal pores

	Numerical results	Roberts–Garboczi [15]
E/E_m ($w = 0.25$)	0.732	0.739
G/G_m ($w = 0.25$)	0.754	0.758

3. Analytical estimates and comparison with numerical results

In this section, focus is given on some analytical estimates to the case of randomly distributed ellipsoidal pores (in space and in orientation).

3.1. Hashin–Shtrikman estimates

The variational representation proposed by Hashin and Shtrikman [6] is based on the use of polarization fields related to an homogeneous reference material. The heterogeneous problem on the RVE is then replaced by a homogeneous thermo-elastic problem involving a polarization field $\tau(x)$:

$$\sigma(x) = C(x) : \varepsilon(x) = C_0 : \varepsilon(x) + \tau(x), \quad \forall x \in Y, \tag{7}$$

where C_0 is the elastic stiffness of the reference material. Assuming that $\tau(x)$ is piecewise constant in a two-phases material subjected to an uniform strain field ε_0 at infinity, the strain field ε_j in the phase j is related to the macroscopic strain $\langle\varepsilon\rangle$ as follows:

$$\langle\varepsilon\rangle = \sum_{j=1,2} c_j\varepsilon_j = \left(\sum_{j=1,2} c_j T_j\right) : \varepsilon_0, \tag{8}$$

where c_j are the volume fraction of the phase j and T_j are defined as

$$\varepsilon_j = T_j : \varepsilon_0. \tag{9}$$

Localization tensors of Hashin–Shtrikman A_j^{HS} are therefore

$$\varepsilon_j = T_j : \left(\sum_{j=1,2} c_j T_j\right)^{-1} : \langle\varepsilon\rangle = A_j^{\mathrm{HS}} : \langle\varepsilon\rangle. \tag{10}$$

Tensors T_j depend on the choice of C_0. Since overall isotropy is investigated (randomly oriented inclusions), pertinent localization tensors are orientational averages of T_j denoted by

$$F_j(C_0) = \langle T_j(C_0)\rangle. \tag{11}$$

For ellipsoidal inclusions, tensors T_j are transversely isotropic:

$$T_j = \alpha_j E_{\mathrm{L}} + \beta_j J_{\mathrm{T}} + 2\mu_{tj} K_{\mathrm{T}} + 2\mu_{lj} K_{\mathrm{L}} + \gamma_j F + \gamma_j'^{T} F, \tag{12}$$

where $E_{\mathrm{L}} = n \otimes n \otimes n \otimes n$, $i_{\mathrm{T}} = i - n \otimes n$, $J_{\mathrm{T}} = (1/2) i_{\mathrm{T}} \otimes i_{\mathrm{T}}$, $I_{\mathrm{T}} = I + E_{\mathrm{L}} - 2(n \otimes i \otimes n)_s$, subscript '$s$' denotes the symmetric part, $K_E = (1/6)(2n \otimes n - i_{\mathrm{T}}) \otimes (2n \otimes n - i_{\mathrm{T}})$, $F = (i_{\mathrm{T}} \otimes n \otimes n)/\sqrt{2}$, $K_{\mathrm{L}} = K - K_{\mathrm{T}} - K_E$, $K_{\mathrm{T}} = I_{\mathrm{T}} - J_{\mathrm{T}}$, and α_j, β_j, μ_{tj}, μ_{lj}, γ_j, γ_j' are the elastic moduli (Wapole's notations [20]). Orientational average of any transversely isotropic reads [1,3,8]:

$$\begin{aligned} F_j &= \frac{1}{3}(\alpha + 2\beta + \sqrt{2}(\gamma + \gamma'))J \\ &\quad + \frac{1}{15}(2\alpha + \beta - \sqrt{2}(\gamma + \gamma') + 12(\mu_t + \mu_l))K \\ &= \mathrm{Proj}_{\{J,K\}}(T_j). \end{aligned} \tag{13}$$

This equivalence between orientational average and projection on the isotropy basis is true for any fourth order tensor. This can be proved as follows.

Let us consider two Eshelby's problems (infinite isotropic matrix) where the orientation of inclusions are characterized respectively by a vector n and a vector $\tilde{n}$ and whose displacement solution are denoted respectively by u and by $\tilde{u}$. The strain field ε (respectively $\tilde{\varepsilon}$) in the inclusion is related to the strain field at infinity ε_0 (respectively $\tilde{\varepsilon}_0$) by $\varepsilon = T : \varepsilon_0$ (respectively $\tilde{\varepsilon} = \widetilde{T} : \tilde{\varepsilon}_0$). Since $\tilde{u}$ is a rotation of u ($\tilde{u} = Q \cdot u$, where components of the second-order tensor Q are direction cosines), we thus obtain:

$$\widetilde{T}_{rstp} = Q_{ri} Q_{sj} Q_{tk} Q_{pl} T_{ijkl}. \tag{14}$$

This relation shows that tensors T and $\widetilde{T}$ have the same invariants. The average of T on all orientations has then the same invariant as T too. If all orientations have the same probability (random media), the resulting overall isotropy imposes that the orientational average $\langle T\rangle$ is isotropic. This isotropic tensor having the same invariant as T, one obtains

$$\langle T\rangle = \mathrm{Proj}_{\{J,K\}}(T). \tag{15}$$

Therefore, the Hashin–Shtrikman estimates are for a two-phases material with randomly oriented ellipsoidal inclusions:

$$\begin{aligned} C^{\mathrm{HS}} &= C^{\mathrm{HS}}(C_0) \\ &= \left(\sum_{j=1,2} c_j C_j : F_j(C_0)\right) : \left(\sum_{j=1,2} c_j F_j(C_0)\right)^{-1}, \end{aligned} \tag{16}$$

with

$$F_j(C_0) = \mathrm{Proj}_{\{J,K\}}(T_j(C_0)), \tag{17}$$

where C_j is the elastic tensor of the phase j and where the values of $F_j(C_0)$ are given in [1] for oblates and prolates ellipsoids, for spheres, and for limit cases of needles and penny shape. In the case of ellipsoids, the values of $F_j(C_0)$ were first given by Kröner [7] and by Wu [21]. Various choices of C_0 lead to various estimates as detailed in the following.

The Mori–Tanaka estimate [12] is obtained by taking the matrix as reference material $C_0 = C_m$ (subscript i holds for cavities and m for matrix):

$$C^{MT} = C^{HS}(C_m) = (1-f)C_m : F_m(C_m) : ((1-f)F_m(C_m) + fF_i(C_m))^{-1}. \quad (18)$$

The self-consistent scheme is obtained by taking the effective elastic tensor as reference material:

$$C^{SC} = C^{HS}(C^{SC}). \quad (19)$$

The dilute case estimate consists of a first order development of (18) with respect to f assuming low porosity ($f \ll 1$):

$$C^{DC} = C_m - fC_m : F_i(C_m). \quad (20)$$

The differential self-consistent estimate of McLaughlin [10] consists in progressively incorporating inclusions in matrix using Eq. (20). The effective elastic tensor is given by the differential equation:

$$\frac{dC^{Diff}(f)}{df} = C^{Diff}(f) : F_i(C^{Diff}(f)), \quad \text{with} \quad C^{Diff}(f=0) = C_m. \quad (21)$$

3.2. Berryman estimate

The Berryman model [1] is a so-called self-consistent model which could be interpreted as a symmetric representation of the Wu's model [21]. Estimating the elastic energy in the matrix and in the inclusions by the total elastic energy, Wu proposes a quasi-self-consistent model where the effective elastic tensor is implicitly defined by

$$C^{Wu} = \overline{C}(C^{Wu}), \quad \text{with} \quad \overline{C}(C_0) = C_m + \sum_{j=1,2} c_j(C_j - C_m) : F_j(C_0). \quad (22)$$

It should be noticed that C^{DC} is equal to $\overline{C}(C_m)$. The lack of symmetry in Eq. (22) is corrected by Berryman by substituting C_0 to C_m. This estimate could then be written as

$$C^{B} = \widetilde{C}(C^{B}), \quad \text{with} \quad \widetilde{C}(C_0) = \left(\sum_{j=1,2} c_j C_j : F_j(C_0)\right) : \left(\sum_{j=1,2} c_j F_j(C_0)\right)^{-1}, \quad (23)$$

which corresponds exactly to the self-consistent estimate: $C^{B} = C^{SC}$.

3.3. Ponte-Castañeda–Willis estimate

The estimate of Ponte-Castañeda and Willis [14] is the first estimate that takes into account the effects of the inclusion shape and those of the distribution of the inclusions separately. Using previous notations, the effective elastic tensor of Ponte-Castañeda and Willis can be written in our case as

$$C^{PCW} = C_m + \left(\left(\sum_{j=i,m} c_j \langle W_j \rangle\right)^{-1} - P_m^d\right)^{-1}, \quad (24)$$

which yields for porous media:

$$C^{PCW} = C_m + ((f\langle W_i \rangle)^{-1} - P_m^d)^{-1}, \quad (25)$$

where $P_m^d = \left\{\frac{1}{3K_m+4G_m}, \frac{3(K_m+2G_m)}{5G_m(3K_m+4G_m)}\right\}$, and $W_i = P^{-1} - P^{-1} : (P^{-1} + C_i - C_m)^{-1} : P^{-1}$, with $\langle P \rangle^{-1} = C_m : F_m(C_m) : (F_i(C_m) - F_m(C_m)) : F_i(C_m)$ and with K_m denoting the bulk modulus of the matrix.

It should be noticed that this estimate is able to take into account the isotropy of the spatial distribution (leading to the isotropy of P_m^d) and the random orientation of the inclusions (leading to the isotropy of $\langle W_i \rangle$). In the case of spherical cavities, this estimate corresponds to the Mori–Tanaka estimate ($P = P_m^d$). In the case of ellipsoidal cavities, C^{PCW} is defined only for density parameters lower than 1 (the density parameter is equal to the product fw^2 when $w > 1$ and to the ratio f/w when $w < 1$).

3.4. Comparison with numerical results

Figs. 6 and 7 show the evolution of Young and shear moduli versus porosity, in the case of spherical cavities. Table 1 shows, at $f = 10\%$, an agreeable comparison between our numerical results and some analytical approaches such as Mori–Tanaka [12] (equivalent to the upper bound of Hashin and Shtrikman for porous materials), quasi-self-consistent Wu's model [21], differential scheme [10], self-consistent scheme and dilute case model ([18] and cited references).

The presented estimates are compared to numerical results on Figs. 8 and 9 in terms of sensitivity to the aspect ratio for a given porosity. In the case of the particular microstructure considered in this paper (low volume

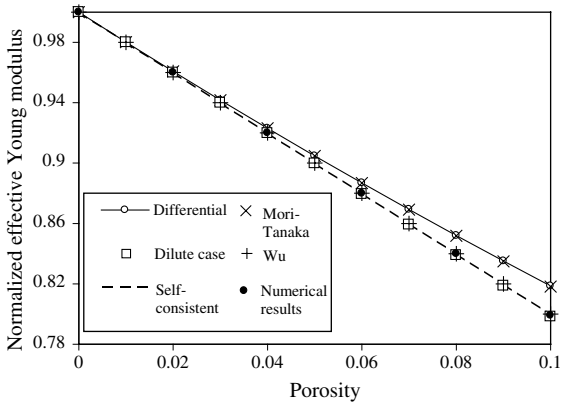

Fig. 6. Effective Young modulus versus porosity (spherical pores): comparison between various estimates and numerical results.

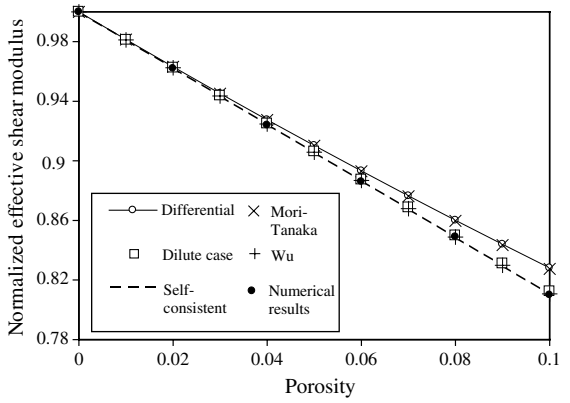

Fig. 7. Effective shear modulus versus porosity (spherical pores): comparison between various estimates and numerical results.

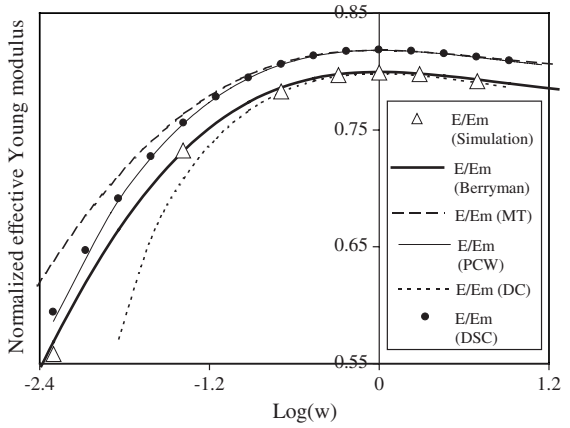

Fig. 8. Comparison between numerical results and various estimates (Berryman, Mori–Tanaka (MT), dilute case (DC), differential self-consistent (DSC), Ponte-Castañeda–Willis (PCW)) for spherical and ellipsoidal pores at $f = 10\%$: normalized effective Young modulus versus aspect ratio for density parameter lower than 1.

fraction of ellipsoidal pores randomly distributed in space and in orientation in an elastic and isotropic matrix), the self-consistent estimate (Berryman estimate, see Section 3.2) is the most accurate estimate in terms of Young and shear moduli. This result confirms the observations of [3].

4. Experimental approach

4.1. Micro-acoustic approach

The elastic properties of a material can be assessed by using different experimental methods (compressive tests,

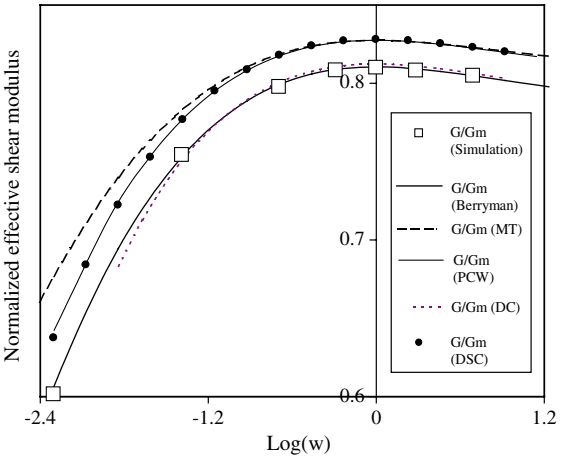

Fig. 9. Comparison between numerical results and various estimates (Berryman, Mori–Tanaka (MT), dilute case (DC), differential self-consistent (DSC), Ponte-Castañeda–Willis (PCW)) for spherical and ellipsoidal pores at $f = 10\%$: normalized effective shear modulus versus aspect ratio for density parameter lower than 1.

resonant methods, etc.). However, although these experiments are very efficient on many materials, they generally fail on UO_2 because after irradiation, the pellet is entirely fractured and spread in pieces, thus exhibiting a steep radial gradient in physical properties. That is the reason why other local approaches such as the focalized ultrasonic methods are considered as interesting and powerful tools.

Non-destructive testing [13] is usually performed on large zones (about 1 cm^2) with the help of plane sensors. As the uranium dioxide pellets are quite small (about 8 mm) and non-homogeneous in the case of irradiated samples, one has to use more local methods: high frequency acoustic microscopy or micro-echography. General aspects of these two methods are developed in the following discussion. More details can be obtained from [16,17].

Ultrasonic waves generated by a piezoelectric crystal are focused on the sample by a spherical lens (Fig. 10). These waves, that are transmitted through a coupling fluid (ethanol or methanol for UO_2 study), are reflected on the sample, collected again by the piezoelectric crystal interfering with the specular beam and converted into an electric signal. If a plane X–Y scan is performed, acoustical pictures can be obtained if the electrical signal which is acquired by the piezoelectric is encoded in color levels. Doing so, the spatial resolution ranges from 100 μm (operating frequency 15 MHz) to 1 μm if very high frequencies are used (600 MHz).

Even if the acoustical pictures give interesting qualitative information concerning the reflection power of the sample (which is a function of the density and the

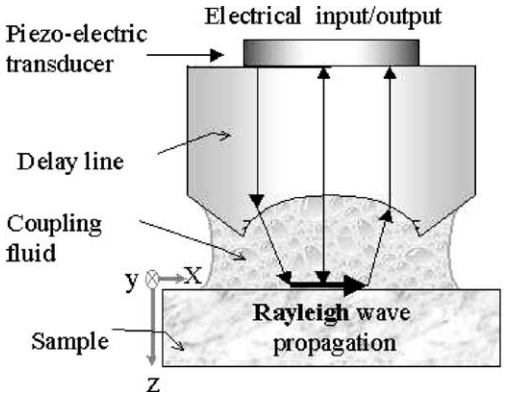

Fig. 10. Schematic representation of an acoustic sensor used in acoustic microscopy.

ultrasonic waves velocities), quantitative results are obtained with the so-called acoustic signature $V(z)$. For $V(z)$ acquisitions, the sensor is de-focused, which means gradually approached towards the surface sample. Surface waves are then created and interference phenomena are observed between reflected surface waves and the specular beam with a normal incidence.

The amplitude of the electric signal acquired, recorded versus the length of defocusing z, is called the acoustic signature. Distance between two peaks provides the propagation velocity of the wave reflected.

During the defocusing, the surface analyzed on the sample becomes larger. For most materials, it can be considered that this zone is equal to the half length of defocusing. This represents 1 mm if the operating frequency is 15 MHz, 300 μm for experiments at 150 MHz and 30 μm for high frequencies (500 MHz). In the case of UO_2, 150 MHz seems to be a reasonable frequency: using higher frequencies is tricky because of attenuation processes.

It seems that two pseudo periods are present in the $V(z)$: one due to the Rayleigh wave and one due to the longitudinal surface wave. The measurement of these pseudo periods then gives the Rayleigh and the longitudinal waves velocities (accuracy 10 m/s) [4].

From the longitudinal velocity (V_L) and the Rayleigh wave velocity (V_R), we deduce the transverse velocity (V_T), which is solution of the polynomial (26) [19], with respect to the condition (27). The elastic moduli are then deduced from Eqs. (28) and (29)

$$V_T^8 - (V_L^2 + V_R^2)V_T^6 + \frac{3}{2}V_L^2V_R^2V_T^4 - \frac{1}{2}V_L^2V_R^4V_T^2 + \frac{1}{16}V_L^2V_R^6 = 0, \tag{26}$$

$$0 \leqslant V_T \leqslant \frac{V_L}{\sqrt{2}}, \tag{27}$$

$$E = \frac{3V_L^2 - 4V_T^2}{V_L^2 - V_T^2}\rho V_T^2, \tag{28}$$

$$G = \rho V_T^2, \tag{29}$$

where ρ is the density of the considered material.

In the case of UO_2, the efficiency of the longitudinal mode is too low and the measurement of the longitudinal wave velocity by acoustic microscopy generally fails. To overcome this problem, a special device, so-called the micro-echography, has been used.

Traditional echography, usually applied in reflection mode is not adapted to UO_2 because the thickness of the sample is not accurately known.

Our method, called acoustic micro-echography in reflection–transmission mode uses two sensors and four acoustic travels: one transmitted into the water tank, one transmitted through the sample and two echoes reflected on the two parallel faces of the sample (a photography of the device is given on Fig. 11). Thanks to the measurement of four times of flight between the signals, the longitudinal wave velocity is obtained (accuracy 10 m/s). Typical frequencies are about 40 MHz and the analyzed zone on the samples is about 500 μm. The recent measurements on highly porous samples have shown that using higher frequencies and working on smaller zones should be possible.

4.2. Experimental results

The experimental results are given in Fig. 12. Elastic moduli are deduced through Eqs. (28) and (29) using $\rho = 10\,960(1 - f)$ kg/m^3. Experimental uncertainties on these results are very small according to a linear regression for $f \to 0$, which leads to the theoretical elastic moduli of the massive UO_2 ($E_m = 222$ GPa and $G_m = 84$ GPa).

At $f = 10\%$, the values of the measured elastic moduli are given in Table 3 and compared to those of Martin [9] which are mean values on various nuclear pellets including different types of processing. So, without more information on UO_2 used, Martin approximation is validated.

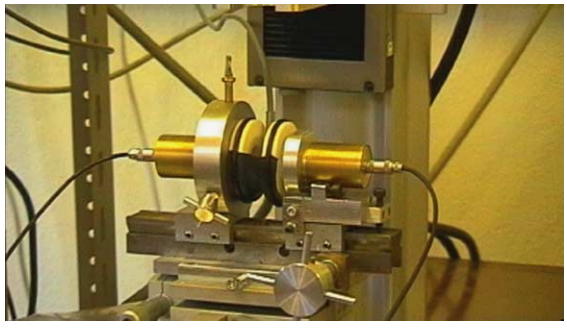

Fig. 11. Photography of the micro-echographic device.

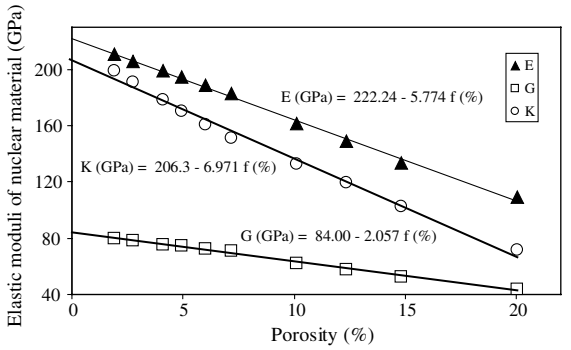

Fig. 12. Experimental data: elastic moduli of nuclear material versus porosity.

Table 3
Effective elastic moduli of the nuclear pellet material: comparison of experimental data at $f = 10\%$ between our results (linear interpolation) and Martin's data [9] (linear regression of various UO_2 nuclear pellet materials)

	E/E_m	G/G_m
Experimental results	0.738	0.752
Martin [9]	0.750	0.775

5. Overall elastic properties of nuclear pellet

The UO_2 nuclear ceramics contain both spherical (intra-granular) cavities and ellipsoidal (inter-granular) cavities. This paragraph investigates the case of a single population of cavities (spherical or ellipsoidal) and the case of a bi-modal microstructure (spherical and ellipsoidal). This last case mimics the 'real' microstructure of UO_2 nuclear pellets.

5.1. Single population of cavities

5.1.1. Spherical cavities

Fig. 12 shows the Young and the shear moduli versus porosity (range of porosity [0–20%]). It should be noted, as already underlined by [9] for instance, that these evolutions can be accurately approximated by a linear function as in Eq. (30)

$$\begin{cases} \dfrac{G}{G_m} \approx 1 - \alpha_{Gs} f, \\ \dfrac{E}{E_m} \approx 1 - \alpha_{Es} f, \end{cases} \tag{30}$$

where α_{Es} and α_{Gs} are non-negative constants (see Table 5) assumed to be independent of the matrix properties [9].

For a porosity lower than 10%, most of the analytical models for porous media also give quasi-affine relation between porosity and normalized effective elastic moduli but predict a dependence of the quantities α_{Es} and α_{Gs} on the matrix properties. The aforementioned independence of those quantities to matrix properties in empirical fits can be checked here by studying the sensitivity of α_{Es} and α_{Gs} to matrix properties in an acceptable range of variations of the UO_2 matrix properties. The main parameter governing those variations in nuclear reactors is the temperature. Since the Young and shear moduli of the UO_2 matrix have a quadratic dependence with temperature (Eq. (31), from [9]), we check on Table 4 that quantities α_{Es} and α_{Gs} do not significantly vary between $T = 273\,\mathrm{K}$ and $T = 2000\,\mathrm{K}$: considering α_{Es} and α_{Gs} as constants is thus a convenient assumption. This result could be explained by a very small variation of the Poisson ratio with temperature: between $T = 273\,\mathrm{K}$ and $T = 2000\,\mathrm{K}$, the Young and the shear moduli decrease about 30%, while the Poisson ratio only decreases of about 5%:

$$\begin{cases} G_m(T) = 2.2693 \times 10^2 - 1.5399 \times 10^{-2} T \\ \qquad\qquad -9.597 \times 10^{-6} T^2, \\ E_m(T) = 85.83 - 5.157 \times 10^{-3} T - 3.747 \times 10^{-6} T^2, \end{cases} \tag{31}$$

where elastic moduli are expressed in GPa and temperature in Kelvin.

Eq. (30) could be rewritten as $G(T,f) \approx G_m(T)(1 - \alpha_{Gs} f)$ and $E(T,f) \approx E_m(T)(1 - \alpha_{Es} f)$. Since constants α_{Es} and α_{Gs} are independent of the matrix properties, several populations of spherical cavities (sorted by growing radii and having porosity f_1 to f_{Nt}) could be treated in a simple incremental way: assuming that the total porosity is small, effective Young modulus is obtained by Eq. (32). The same result holds for the effective shear modulus

$$\frac{E}{E_m} = \prod_{i=1}^{Nt} (1 - \alpha_{Es} f_i) \approx \left(1 - \alpha_{Es} \sum_{i=1}^{Nt} f_i\right) = (1 - \alpha_{Es} f). \tag{32}$$

Table 4
Numerical solution for spherical pores to study the influence of the evolution of the matrix properties (with respect to the temperature) on effective properties

	E/E_m	G/G_m
Matrix at 273 K	0.799	0.810
Matrix at 2000 K	0.799	0.808

Table 5
Comparison of α_E and α_G between our results for spherical and ellipsoidal pores, Martin's data and micro-acoustic data

	α_E	α_G
Spherical cavities	2.03 ± 0.02	1.92 ± 0.05
Ellipsoidal pores ($w = 0.25$)	2.68 ± 0.02	2.46 ± 0.02
Martin	2.5	2.25
Micro-acoustic	2.62	2.48

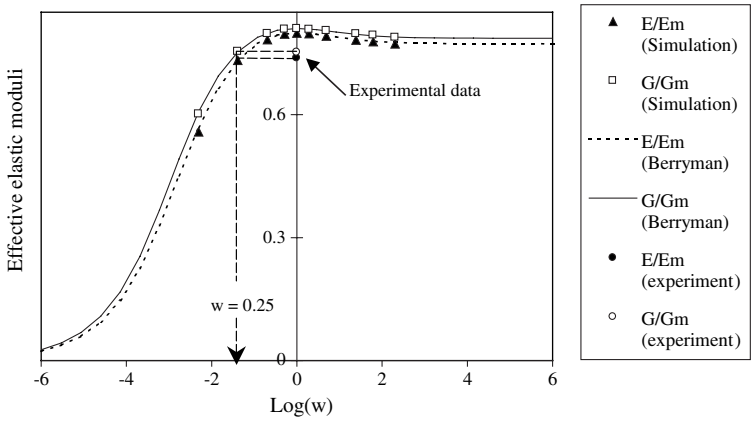

Fig. 13. Comparison between numerical results, Berryman estimate and experimental data for spherical and ellipsoidal pores at $f = 10\%$: normalized effective elastic moduli versus aspect ratio.

5.1.2. Ellipsoidal cavities

Assuming that the microstructure only contains ellipsoidal cavities with the same aspect ratio, Fig. 13 shows that no prolates could be considered in the UO_2 material (the asymptotic limit of the needles shape corresponds to elastic moduli larger than measured elastic moduli). Experimental data is obtained for oblates having an aspect ratio about 0.25.

5.2. Bi-modal population of cavities

Since both populations of spherical and ellipsoidal cavities are present in nuclear material, the retained self-consistent analytical estimate (see Section 3.4) could be used as an inverse method to determine convenient couple of aspect ratio of ellipsoidal cavities and volume fraction of spherical cavities leading to the effective shear modulus measured by micro-acoustic experiments. This study is performed for 10% of total porosity (i.e. the sum of the volume fraction of spherical cavities and of the volume fraction of ellipsoidal cavities). The previous paragraph shows that for 0% of spherical cavities (a microstructure with 10% of porosities made up only of ellipsoidal inter-granular cavities), the aspect ratio of ellipsoidal cavities is about 0.25. At the opposite, in the case of 100% of spherical cavities (a microstructure with 10% of porosities made up only of spherical intra-granular cavities), Fig. 13 shows that for $w = 1$, experimental data could not be reached.

The convenient couples of microstructural parameters are given on Fig. 14, using remarks on Section 5.1: effective elastic properties of the bi-modal microstructure is obtained by incorporating random ellipsoidal cavities in a new isotropic 'matrix' composed of an UO_2 matrix including spherical cavities randomly distributed. This result shows that both intra-granular and inter-granular cavities have to be taken into account in any accurate micro-mechanical modeling.

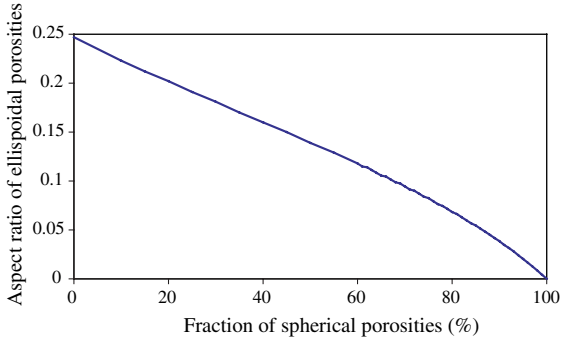

Fig. 14. Aspect ratio of ellipsoidal pores population versus fraction of spherical pores for a total porosity of 10% in the case of bi-modal microstructure.

6. Concluding remarks

Using a technique of periodic homogenization, we have determined effective elastic properties of porous ceramics including spherical and ellipsoidal cavities randomly distributed in space and orientation. Numerical results were given for various porosities in the case of spherical cavities, and for various shapes in the case of a 10% porous ceramic with ellipsoidal pores. Normalized effective properties were thus given as a function of the aspect ratio of ellipsoidal pores. Various analytical estimates were derived from literature. Our simulations show that the self-consistent estimate is the best accurate model for the considered type of microstructure.

In the case of UO_2 fuel material, comparison of the analytical–numerical estimates to the micro-acoustic experimental data shows that:

- The usual empirical fits of Martin [9] performed on a wide range of bibliographic data give accurate estimates of elastic properties.

- Agreement with experimental data cannot be reached unless including a population of ellipsoidal pores (inter-granular cavities).
- Assuming that inter-granular pores have ellipsoidal shapes, their aspect ratio is lower than about 0.25 (penny shaped oblates).

Acknowledgments

The authors are grateful to Dr J.-C. Michel and Dr H. Moulinec of the Laboratoire de Mécanique et d'Acoustique, CNRS UPR7051, for helpful comments on numerical methods of periodic homogenization for random media.

References

[1] J.G. Berryman, Appl. Phys. Lett. 35 (1979).
[2] J.G. Berryman, J. Acoust. Soc. Am. 68 (1980).
[3] D. Bonnenfant, F. Mazerolle, P. Suquet, Mech. Mater. 29 (1998) 93.
[4] A. Briggs, Acoustic Microscopy, Clarendon, Oxford, 1922.
[5] E.J. Garboczi, K.A. Snyder, J.F. Douglas, M.F. Thorpe, Phys. Rev. E 52 (1995) 819.
[6] Z. Hashin, S. Shtrikman, J. Mech. Phys. Solids 11 (1963) 127.
[7] E. Kröner, Z. Phys. 151 (1958) 504.
[8] D. Laux, G. Despaux, D. Baron, J. Spino, in: Proceedings of 7ième conférence internationale sur les combustibles CANDU, 2001.
[9] D.G. Martin, High Temp. High Press. 21 (1989) 13.
[10] R. McLaughlin, Int. J. Eng. Sci. 15 (1977) 237.
[11] J.-C. Michel, H. Moulinec, P. Suquet, Comput. Meth. Appl. Mech. Eng. 172 (1999) 109.
[12] T. Mori, K. Tanaka, Acta. Metall. Mater. 21 (1973) 597.
[13] J.L. Pelletier, La pratique du contrôle industriel par ultrasons, ENSAM, 1979.
[14] P. Ponte-Castañeda, J.R. Willis, J. Mech. Phys. Solids 43 (1995) 1919.
[15] A.P. Roberts, E.J. Garboczi, J. Am. Ceram. Soc. 83 (2000) 3041.
[16] A.P. Roberts, M. Teubner, Phys. Rev. E 51 (1995) 4141.
[17] V. Roque, D. Baron, J. Bourgoin, J.-M. Saurel, J. Nucl. Mater. 275 (1999) 305.
[18] S. Torquato, Random Heterogeneous Materials, Springer-Verlag, New York, 2002.
[19] I.A. Viktorov, Rayleigh and Lamb Waves, Plenum, New York, 1967.
[20] J.L. Walpole, J. Mech. Phys. Solids 17 (1969) 151.
[21] T.T. Wu, Int. J. Solid Struct. 2 (1966) 1.